Research Article Vol. 11, No. 1 / January 2024 / Optica 81

OPTICA

# Ultra-broadband quantum infrared spectroscopy

Toshiyuki Tashima,[1] Yu Mukai,[1] Masaya Arahata,[1] Norihide Oda,[1] Mamoru Hisamitsu,[2] Katsuhiko Tokuda,[2] Ryo Okamoto,[1] and Shigeki Takeuchi[1,*]

[1]Department of Electronic Science and Engineering, Kyoto University, Kyotodaigakukatsura, Nishikyo-ku, 615-8510 Kyoto, Japan
[2]Shimadzu Corporation, 3-9-4, Hikaridai, Seika-cho, Soraku-gun, 619-0237 Kyoto, Japan
*takeuchi@kuee.kyoto-u.ac.jp

Received 31 August 2023; revised 27 November 2023; accepted 1 December 2023; published 12 January 2024

**Spectroscopy in the mid-infrared region is an indispensable tool for identifying molecular types in various fields, including physics, chemistry, and medical sciences. However, conventional infrared light sources, detectors, and noise from blackbody radiation have been the obstacles to miniaturization and higher sensitivity of infrared spectrometers. Quantum infrared spectroscopy, which uses visible and infrared photon pairs in a quantum entangled state, has attracted attention as a new sensing technology that enables infrared spectroscopy with detectors in the visible range. However, the bandwidth of conventional quantum entangled light sources is at most 1 μm or less, which hinders broadband measurements, which are important in spectroscopic applications. Here we have realized an ultra-broadband entangled state of visible–infrared photons with wavelengths from 2 to 5 μm, harnessing a specially designed nonlinear crystal with chirped poling structure inside. Furthermore, we constructed a nonlinear quantum interferometer using the ultra-broadband quantum entangled photons and realized broadband infrared spectroscopy of inorganic and organic materials using a visible detector made of silicon. Our results show that quantum infrared spectroscopy can achieve ultra-broadband spectroscopic measurements and pave the way for the highly sensitive, ultra-compact infrared spectrometers using quantum entangled photons.** 

https://doi.org/10.1364/OPTICA.504450

## 1. INTRODUCTION

Infrared (IR) spectroscopy is a versatile tool in a broad range of fields from astronomy to medicine [1]. The transmission spectrum reflects the vibrational modes unique to the molecules in a sample and is thus widely used to discriminate materials. The current state-of-the-art IR spectroscopy technique is Fourier transform IR (FTIR) spectroscopy. However, the relatively low efficiency of available IR sources and detectors has been an obstacle for the development of FTIR spectroscopy, such as efforts to miniaturize FTIR systems. One way to solve the problem is by improving mid-IR (MIR) thermal light sources and detectors. Quantum cascade lasers (QCLs) in the MIR region have been investigated, but the bandwidth of off-the-shelf QCLs is still limited [2]. Further, high-sensitivity MIR detectors often require cryogenic cooling and are subject to export control [3].

Recently, photonic quantum sensing harnessing quantum entanglement and/or quantum nonlinear interference has been attracting attention [4–19]. In particular, a prominent demonstration of the absorption measurement in the infrared region using a visible light source and a detector was performed [4–11,17] using a nonlinear interferometer [20,21]. Since this novel method, quantum infrared spectroscopy (QIRS) [4], requires neither a light source nor a detector in the MIR region, it is a promising candidate for a compact and low-cost novel MIR spectrometer. Following this demonstration, the concept of quantum FTIR (QFTIR) spectroscopy was reported [6,8].

A shortcoming of these demonstrations of QIRS is the limited spectral coverage [4–11]. To address this problem, the broadband group-velocity phase matching aimed to use for QIRS has been demonstrated; however, the bandwidth was still smaller than 1 μm [22]. Alternatively, wavelength tunable QIRS systems have been recently realized by tuning the angle of a nonlinear crystal [5,23] or the crystal temperature [24], but with the drawback of a long measurement time required for the wavelength tuning process.

Here, we experimentally demonstrate the QIRS with an ultra-broadband frequency-entangled photon pair source using chirped quasi-phase-matched periodically poled magnesium doped stoichiometric lithium tantalate (PPMg:SLT). We successfully observed an ultra-broad spectrum of visible signal photons from 595 to 725 nm, which corresponds to wavelengths of the idler photons from 2.0 to 5.0 μm with a bandwidth of 3.0 μm. Then we constructed a quantum nonlinear interferometer in the low-gain regime where the average photon flux is below one photon pair per correlation time for the biphotons. We successfully observed a quantum interferogram and obtained an MIR broadband spectrum of the idler photons. Finally, we performed ultra-broadband QFTIR spectroscopy over the range of 2.5 to 4.5 μm with a bandwidth of 2.0 μm for solid and liquid samples.

This demonstration of ultra-broadband QFTIR spectroscopy covering the whole MIR region, using a visible light source and detector, paves the way for its use in a wide range of fields from materials science to medical applications.

## 2. DEVELOPMENT OF AN ULTRA-BROADBAND CHIRPED QPM DEVICE

To realize the ultra-broadband visible and MIR entangled photon-pair source, we developed a chirped quasi-phase-matching (QPM) device [25,26] with a spatially modulated QPM structure to generate broadband two-photon states by continuously varying the phase-matching condition. For comparison, we also experimentally evaluated a non-chirped QPM device with uniform poling periods suitable for generating photon pairs at specific wavelengths with relatively narrow spectral bandwidths. In the following, we compare the experimentally obtained emission spectra of visible photons from both devices with theoretical calculations to confirm that photon pair generation occurs in the desired spectral regions. The QPM device uses PPMg:SLT [25–34]. This nonlinear optical material is not subject to instability in short-wavelength pumping [35], has a transmission region from ultraviolet to mid-infrared wavelengths [36], and has a high damage threshold of the order of $GW/cm^2$.

Figure 1(a) shows a schematic view of the non-chirped QPM device. The dimensions of the device are $1 \times 1 \times 10\ mm^3$. The spatial frequencies of the polarization reversals for the segment $\Gamma$, corresponding to the inverse of the poling periods, are set based on a previously reported equation [33]. $1/\Gamma$ is set to 12.9 μm. The QPM structure is designed to generate a photon pair with a visible wavelength of 612 nm and an infrared wavelength of 4100 nm via collinear type-0 spontaneous parametric down-conversion (SPDC), assuming a crystal temperature of 30°C and an excitation wavelength of 532.45 nm. The refractive index of Mg:SLT is modeled by the Sellmeier equation [25]. The calculated emission spectrum of the photon pair, shown in Fig. 1(b), is centered at the designed wavelengths and has a spectral width of 0.4 nm full width at half maximum (FWHM) for a visible signal photon. The experimentally observed emission spectrum of the signal photons has a peak with a FWHM of 0.7 nm, centered at the designed wavelength, as shown in Fig. 1(c). Compared to the simulation result, the experimental data have a slightly larger spectral width due to the finite wavelength resolution of the visible spectrometer (0.17 nm).

Figure 1(d) shows the chirped QPM device consisting of 50 segments with different poling periods for simultaneously generating photon pairs with a variety of combinations of wavelengths. The dimensions of the device are $1 \times 1 \times 10\ mm^3$. The QPM structure is designed so that the emission spectrum of a photon pair is continuously distributed in the wavelength range of 595 to 725 nm in the visible region and 2 to 5 μm in the infrared region. For the device used in this work, the number of segments $n$ is 50, and $1/\Gamma$ (1) and $1/\Gamma(n)$ are set to 9.58 and 13.33 μm, respectively, corresponding to a chirp rate of 39.1.

Figure 1(e) shows numerical simulation results for the emission spectrum of a photon pair generated from the chirped device, assuming a pump wavelength of 532.45 nm and a crystal temperature of 55.1°C. In this simulation, we considered that each segment has a finite length and is assumed to be a step function to reflect the actual QPM structure. The calculation results show that the spectral intensity of SPDC photons generated from the chirped device is distributed over a much wider bandwidth than that from the non-chirped device. Visible signal photons are generated in the wavelength range of 595–725 nm, and infrared idler photons in the wavelength range of 2.0–5.0 μm. Fine ripples are seen throughout the spectrum, which can be attributed to quantum interference between the photon-pair generation processes in the different segments [37]. In the experiment, we measured the emission spectrum of visible signal photons generated from the chirped QPM device using the visible spectrometer. Here, the pump power was set to 150 mW and the emission spectrum was accumulated 60 times with an exposure time of 1 s. As shown in Fig. 1(f), we succeeded in observing broadband generation of SPDC photons, ranging from 595 to 725 nm, equal to the bandwidth of the numerical simulation (126 nm).

To evaluate the SPDC photon generation rate for the chirped QPM device, we measured the pump power dependence of the signal photon count rate, which increased linearly with increasing pump power. The generation rate for the signal photons collected through the multimode fiber to the single photon detector, was estimated to be larger than $2.5 \times 10^4$ photons/mW. These results clearly show that the chirped QPM device is a highly efficient entangled photon pair source suitable for broadband quantum infrared spectroscopy.

## 3. EXPERIMENTAL DEMONSTRATION OF ULTRA-BROADBAND QIRS

### A. Experimental Setup

We constructed the QIRS system by a Michelson-type nonlinear quantum interferometer using the Mg:SLT QPM device and confirmed that a quantum interferogram can be obtained over the entire bandwidth of the generated photon pairs. Figure 2(a) shows the interferometer. In the experimental setup in Fig. 2(a), a pump light passes through the QPM device twice so that quantum interference between two photon-pair generation processes occurs. The QPM device is placed in an oven and set to the optimum operating temperature by a temperature controller (OV30D+TC-038D, HC Photonics). A continuous-wave laser with a wavelength of 532.45 nm (Cobolt Samba, output power 300 mW, linewidth $\leq 1$ MHz) is used as the pump source. The polarization of the pump light is adjusted by a halfwave plate (HWP). After being reflected by a dichroic mirror with a 567 nm cutoff wavelength (DM1, DMLP567 Thorlabs), the pump light is focused on the center of the QPM device with a lens (Len, $f = 200$ mm) generating visible–MIR photon pairs. The focused beam diameter is 100 μm. The visible signal photons and the pump light are transmitted through the second dichroic mirror with a 2000 nm cutoff wavelength (DM2, Optical Coatings Japan) and again focused onto the QPM device by a concave mirror (CM). The infrared idler photons are reflected by DM2 and spatially separated from the pump light and the signal photons. After being collimated by an off-axis parabolic mirror (OAPM, $f = 150$ mm), the idler photons pass through a germanium window (G), are reflected by an end mirror (Mi), and are finally refocused by the OAPM onto the QPM device. Mi is placed on a high-precision translational stage (FS-1020UPX, Sigma Koki) to adjust the idler path length. Then, quantum interference between the photon pair generation processes occurs when the spatial modes of the first SPDC photons match those of the second SPDC photons. The signal photons

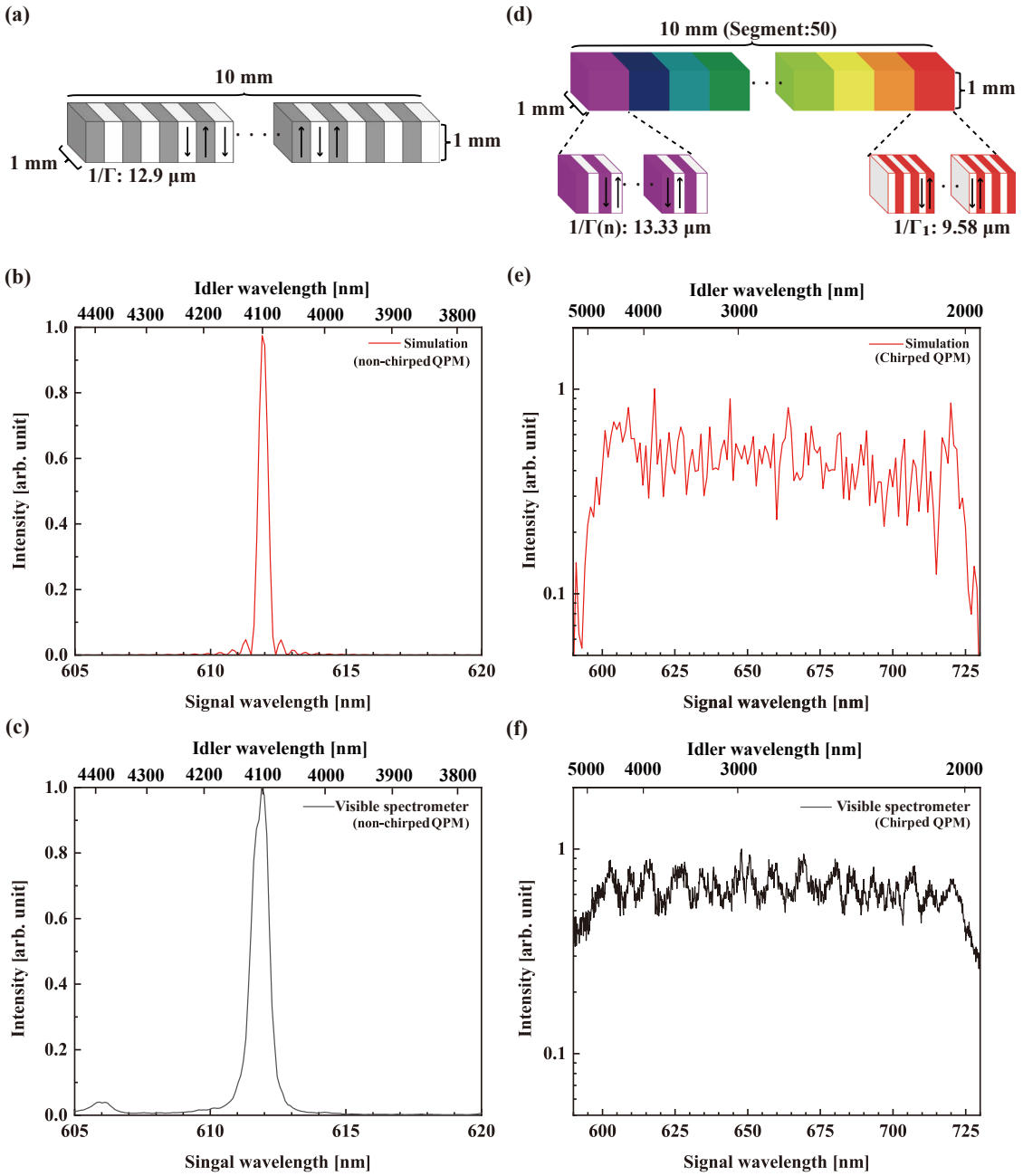


**Fig. 1.** Optical characteristics of non-chirped and chirped QPM devices. The material of QPM devices is Mg-doped stoichiometric lithium tantalate (Mg:SLT). The crystal length is 10 mm. The height and width are 1 mm. (a) Schematic view of a non-chirped QPM device. The wavelengths of visible and MIR photon pairs are 612 and 4100 nm, respectively. (b) Numerical simulation results for expected signal (visible) spectrum for visible and MIR photon pairs generated from the non-chirped QPM device. The lower and upper horizontal axes show signal (visible) and idler (MIR) wavelengths, respectively. (c) Experimental signal (visible) spectrum for visible and MIR photon pairs generated from the non-chirped QPM device. (d) Schematic view of a chirped QPM device. The wavelengths of visible and MIR photon pairs are 595 to 725 nm and 2000 to 5000 nm. (e) Numerical simulation results for expected signal (visible) spectrum for visible and MIR photon pairs generated from the chirped QPM device. (f) Experimental signal (visible) spectrum for visible and MIR photon pairs generated from the chirped QPM device.

pass through DM1 and a long-pass filter with a 550 nm cut-on wavelength and a short-pass filter (SPF) with a 1000 nm cut-on wavelength. To filter out the unwanted luminescent light, a band pass filter (BPF) with a center wavelength of 609 nm and a bandwidth of 20 nm is placed in the case of a non-chirped device, and a BPF with a center wavelength of 665 nm and a bandwidth of 150 nm is placed in the case of a chirped device. After the filters, a pinhole is used to spatially select the center-most part of the signal beam. The pinhole (P) aperture is set at 150 μm for the non-chirped device and 200 μm for the chirped device. Finally, the signal photons are coupled to a multimode fiber guided to a Si avalanche photodetector (SPCM-AQRH-14FC, Excelitas Tech.) and the photon count is recorded with a photon counter (SR400, Stanford Research systems). It is noted that a visible spectrum is also recorded with a dispersive visible spectrometer (SR500i+DU416A-LDC-DD, Andor). The grating groove density and the grating blaze of the spectrometer are 300 l/mm and 1000, respectively. As a result of quantum interference between the

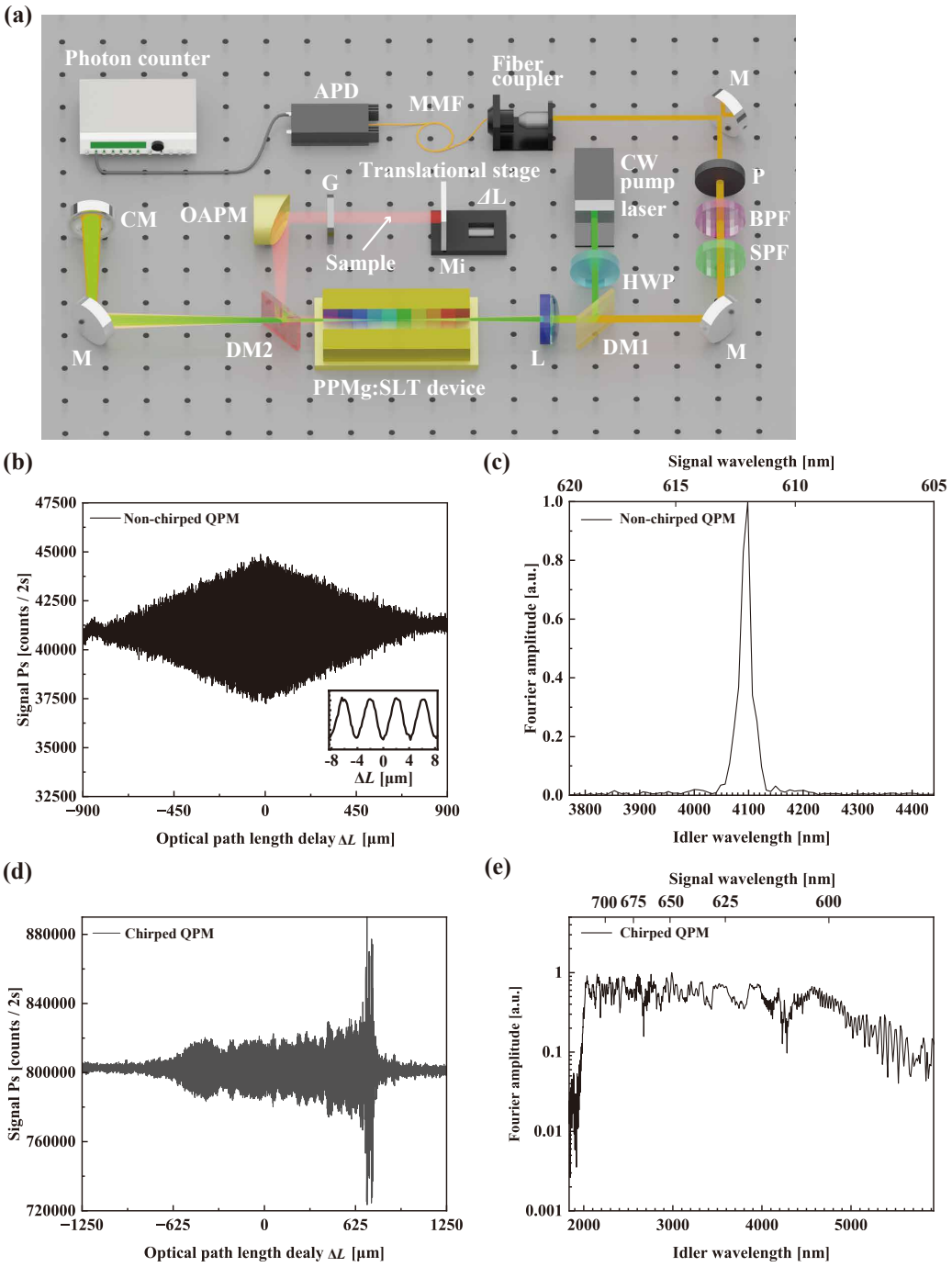


**Fig. 2.** Experimental setup and the evaluation of QFTIR spectroscopy. (a) Schematic view of our experimental setup. Non-chirped or chirped QPM devices are placed on a stage with an oven with a temperature controller. HWP, half-wave plate; DM1, dichroic mirror with 567 nm cutoff wavelength; L, lens, $f = 200$ mm; DM2, dichroic mirror with 2000 nm cutoff wavelength; M, mirror; CM, concave mirror; OAPM, off-axis parabolic mirror, $f = 150$ mm; G, germanium window; Mi, mirror on translational stage; SPF, short-pass filter; BPF, bandpass filter; P, pinhole (150 μm or 200 μm); MMF, multimode fiber; APD, avalanche photodiode (Si). (b) Quantum interferogram obtained from interference between two visible and MIR photon pair generation processes by non-chirped QPM device. The inset shows a part of the magnified quantum interferogram close to the quantum interferogram signal. (c) Fourier amplitude calculated from results in (b). The lower and upper horizontal axes show idler (MIR) and signal (visible) wavelengths. (d) Quantum interferogram obtained from interference between two visible and MIR photon pair generation processes by chirped QPM device. (e) Fourier amplitude calculated from the results in (d).

photon-pair generation processes, the signal photon count varies depending on the optical path length difference $\Delta L$ inside the nonlinear quantum interferometer. In the subsequent measurements, quantum interferograms, i.e., visible signal photon counts, are recorded as a function of $\Delta L$ by translating Mi with a step size of 100 nm (corresponding to $\Delta L$ of 200 nm) up to a total translation distance $W$. At each step, signal counts are integrated for 2 s. By calculating the Fourier spectrum of the quantum interferogram measured in this way, the spectral intensity of the infrared idler

photons contributing to quantum interference can be obtained [6,8].

Figure 2(b) shows a quantum interferogram taken with the non-chirped QPM device. The pump power was set to 180 mW and the average signal photon count was $4.1 \times 10^4$ counts/2s. We observed a distinct interferometric signal showing a periodic oscillation within an approximately 1-mm-wide envelope. The visibility of the signal was $V = (P_{max} - P_{min})/(P_{max} + P_{min}) = 9.1\%$, where $P_{max}$ and $P_{min}$ are the maximum and minimum photon count rates, respectively. As shown in the inset, the oscillation period of the interferogram was about 4 μm, corresponding to the design wavelength of 4100 nm for the idler photons generated by the non-chirped QPM device. We performed a Fourier transform of the quantum interferogram shown in Fig. 2(b) using a fast Fourier transform (FFT) algorithm [6,8]. The wavenumber resolution of the Fourier spectrum $\delta k$ is determined by the reciprocal of the total translation distance, $\delta k = W^{-1}$. In this measurement, $W$ was set to 1.8 mm and the corresponding resolution was $\delta k = 5.6\ \mathrm{cm}^{-1}$. The obtained Fourier amplitude spectrum is shown in Fig. 2(c). A spectral peak is centered around 4100 nm with a FWHM of 0.7 nm. This spectral width is compatible with the numerically calculated idler photon generation bandwidth of 0.4 nm [Fig. 1(b)], indicating that all the spectral components of the photon pair contribute to quantum interference.

Next, we measured a quantum interferogram using the chirped QPM device as a broadband photon-pair source. The total translation distance $W$ was set to 2.5 mm, resulting in a wavenumber resolution $\delta k$ of $4\ \mathrm{cm}^{-1}$ in the Fourier spectrum. The quantum interferogram is shown in Fig. 2(d). The average signal photon count was $8.0 \times 10^5$ counts/2s for a pump power of 150 mW. The visibility was $V = 11.0\%$. The observed quantum interferogram had a highly asymmetric shape and the duration of the signal was much longer than that of the non-chirped QPM device [Fig. 2(b)]. This can be attributed to the chromatic dispersion of the QPM device and germanium window (G) placed on the idler path.

Figure 2(e) shows the Fourier amplitude spectrum of the quantum interferogram in Fig. 2(d). The spectrum is continuously distributed over the entire wavelength range from 2.0 to 5.0 μm, where idler photon generation by the chirped QPM device is expected. The FWHM of the spectrum is 2800 nm, which is in good agreement with the numerically calculated generation bandwidth of the idler photon (2700 nm) as shown in Fig. 1(e). These

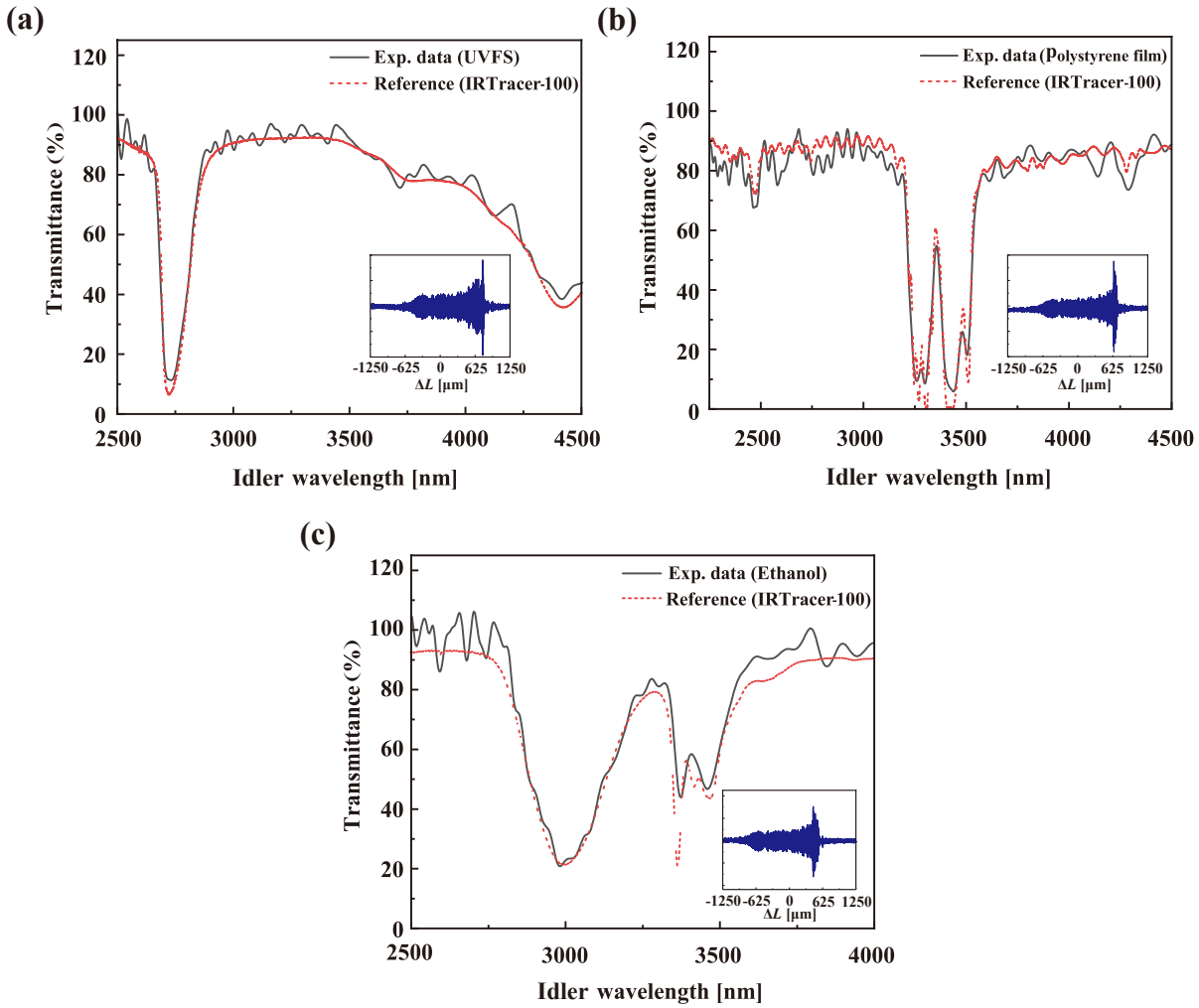


**Fig. 3.** Transmittance measurement of three various samples with an ultra-broadband QFTIR spectroscopy. (a) Transmittance of UVFS, (b) transmittance of polystyrene film, and (c) transmittance of ethanol, calculated from Fourier amplitude obtained by QFTIR spectroscopy. The black line shows the experimental results. The dotted red line shows the reference measured by IRTracer-100 (wavenumber resolution: $4.0\ \mathrm{cm}^{-1}$). The insets show the quantum interferogram obtained from the interference between two visible and MIR photon pair generation processes by a chirped QPM device when the samples are inserted.

results indicate that the fabricated chirped QPM device achieves ultra-broadband QIRS over 1.5 octaves in the MIR region.

### B. Ultra-broadband Transmittance Measurement

To demonstrate the effectiveness of the ultra-broadband QIRS, we measured the transmittance spectra of various samples (fused silica glass, polystyrene film, and liquid-phase ethanol) by QFTIR spectroscopy. In QFTIR spectroscopy, the transmission spectrum of a sample is calculated from the ratio of the Fourier spectra of quantum interferograms measured with and without the sample. Here, apodization was performed throughout the Fourier transform [7]. In the following measurements, the quantum interferograms were acquired over a total translation distance of $W = 2.5$ mm. The precision of a QFTIR measurement can be evaluated from the variation of the measured values in a transmission spectrum taken without a sample ($T \sim 100\%$). From a test measurement, the median and standard deviation of a transmission spectrum in the wavelength range from 2 to 5 μm was estimated to be $99 \pm 4\%$. We used three samples: fused silica glass (1 mm thickness, UV-enhanced fused silica, WG41010, Thorlabs), a polystyrene film (50 μm thickness, Shimadzu Corp), and liquid-phase ethanol (420 nm thickness, 99.5%, FUJIFILM Wako Pure Chemical Corporation). Each sample was inserted between the end mirror (Mi) and the germanium window (G) in the idler path [Fig. 2(a)]. Figure 3 shows the transmission spectrum of each sample measured by QFTIR spectroscopy. As references, the transmission spectra measured by conventional FTIR spectroscopy (IRTracer-100, Shimadzu Corp.) with a wavenumber resolution of 4 $cm^{-1}$ are also shown as red dotted lines. The characteristic IR absorption spectrum of each sample was successfully captured by the QFTIR measurements. The insets in each figure show the change in the shape of the quantum interferogram due to the insertion of the sample.

For the fused silica glass [Fig. 3(a)], we observed an absorption dip around 2700 nm originating from the stretching mode of OH impurities [38] and a broad absorption structure increasing towards long wavelengths.

As shown in Fig. 3(b), a more complex absorption structure for the polystyrene film was also successfully obtained by QFTIR spectroscopy. Polystyrene has multiple absorptions with narrow linewidths; the absorption dips located from 3226 to 3333 nm correspond to C-H stretching modes in the benzene ring, and those from 3333 to 3571 nm can also be assigned to C-H stretching in methylene. The QFTIR results are in fair agreement with the reference data (red dotted line) although the spectrum is averaged to some extent due to the relatively large effective resolution of the QFTIR measurement.

In addition to these solid samples, we measured the transmittance of ethanol samples in the liquid phase. We filled a custom-made 420-nm-gap $CaF_2$ liquid cell with ethanol and measured its transmission spectrum. Figure 3(c) shows the observed absorption peaks derived from an O-H stretching mode centered at 3000 nm and the C-H stretching modes distributed from 3390 to 3509 nm. Although a broadening of the absorption dips is recognized in the QFTIR results, we succeeded in identifying the features of the MIR spectrum of ethanol over a broad spectral range. Note that the modulation of the transmittance due to internal reflection in the liquid cell is so small that it is almost negligible, since the refractive indices of ethanol (1.32) and the $CaF_2$ liquid-cell window (1.42) are close to each other. The transmittance modulation caused by internal reflection is calculated to be less than 0.16%.

## 4. CONCLUSION

In conclusion, we have experimentally demonstrated the QIRS by an ultra-broadband visible–infrared photon pairs with a chirped QPM PPMg:SLT device, where the wavelength of the infrared idler photon ranges from 2.0 to 5.0 μm. Also, we realize the transmittance measurement using ultra-broadband QFTIR spectroscopy using this entangled resource. Our system is capable of measuring characteristic IR spectra for a variety of samples, including fused silica glass, polystyrene films, and liquid-phase ethanol. The QFTIR measurement results obtained over the entire MIR region are in good agreement with the reference data measured by conventional FTIR spectroscopy. The broadband nonlinear quantum interferometry realized in this work will contribute to significant performance improvements not only in quantum infrared spectroscopy, but also in various quantum optical sensing techniques such as quantum imaging and optical coherence tomography with undetected photons, and quantum information processing.

**Funding.** Ministry of Education, Culture, Sports, Science and Technology MEXT Q-LEAP (JPMXS0118067634); Core Research for Evolutional Science and Technology (JPMJCR1674); Cabinet Office, Government of Japan, Public/Private R and D Investment Strategic Expansion Program (PRISM); Precursory Research for Embryonic Science and Technology (JPMJPR15P4); Japan Society for the Promotion of Science (21H04444).

**Acknowledgment.** The authors would like to thank T. Kurita, B. Cao, H. Takashima, and K. Shimazaki for help in preparing the paper.

**Disclosures.** The authors declare no conflicts of interest.

**Data availability.** Data underlying the results presented in this paper are not publicly available at this time but may be obtained from the corresponding author (S. Takeuchi) upon reasonable request.

## REFERENCES

1. P. R. Griffiths and J. A. D. Haseth, *Fourier Transform Infrared Spectrometry*, 2nd ed. (Wiley, 2007).
2. O. Spitz and F. Grillot, "A review of recent results of mid-infrared quantum cascade photonic devices operating under external optical control," J. Phys. Photon. **4**, 022001 (2022).
3. S. Dello Russo, A. Elefante, D. Dequal, D. K. Pallotti, L. Santamaria Amato, F. Sgobba, and M. Siciliani de Cumis, "Advances in mid-infrared single-photon detection," Photonics **9**, 470 (2022).
4. D. A. Kalashnikov, A. V. Paterova, S. P. Kulik, and L. A. Krivitsky, "Infrared spectroscopy with visible light," Nat. Photonics **10**, 98–101 (2016).
5. M. Arahata, Y. Mukai, T. Tashima, R. Okamoto, and S. Takeuchi, "Wavelength-tunable quantum absorption spectroscopy in the broadband midinfrared region," Phys. Rev. Appl. **18**, 034015 (2022).
6. C. Lindner, S. Wolf, J. Kiessling, and F. Kühnemann, "Fourier transform infrared spectroscopy with visible light," Opt. Express **28**, 4426–4432 (2020).
7. C. Lindner, J. Kunz, S. J. Herr, S. Wolf, J. Kießling, and F. Kühnemann, "Nonlinear interferometer for Fourier-transform mid-infrared gas spectroscopy using near-infrared detection," Opt. Express **29**, 4035–4047 (2021).
8. Y. Mukai, M. Arahata, T. Tashima, R. Okamoto, and S. Takeuchi, "Quantum Fourier-transform infrared spectroscopy for complex transmittance measurements," Phys. Rev. Appl. **15**, 034019 (2021).
9. Y. Mukai, R. Okamoto, and S. Takeuchi, "Quantum Fourier-transform infrared spectroscopy in the fingerprint region," Opt. Express **30**, 22624–22636 (2022).
10. C. Lindner, J. Kunz, S. J. Herr, J. Kiessling, S. Wolf, and F. Kühnemann, "Accurate, high-resolution dispersive Fourier-transform spectroscopy with undetected photons," Opt. Contin. **1**, 189–196 (2022).

11. I. Kviatkovsky, H. M. Chrzanowski, E. G. Avery, H. Bartolomaeus, and S. Ramelow, "Microscopy with undetected photons in the mid-infrared," Sci. Adv. **6**, eabd0264 (2020).
12. G. B. Lemos, V. Borish, G. D. Cole, R. L. Sven Ramelow, and A. Zeilinger, "Quantum imaging with undetected photons," Nature **512**, 409–412 (2014).
13. L. A. Rozema, D. H. Mahler, R. Blume-Kohout, and A. M. Steinberg, "Optimizing the choice of spin-squeezed states for detecting and characterizing quantum processes," Phys. Rev. X **4**, 041025 (2014).
14. K. Lyons, S. Pang, P. G. Kwiat, and A. N. Jordan, "Precision optical displacement measurements using biphotons," Phys. Rev. A **93**, 043841 (2016).
15. M. Genovese, "Real applications of quantum imaging," J. Opt. **18**, 073002 (2016).
16. M. Gilaberte Basset, F. Setzpfandt, F. Steinlechner, E. Beckert, T. Pertsch, and M. Gräfe, "Perspectives for applications of quantum imaging," Laser Photon. Rev. **13**, 1900097 (2019).
17. A. Vanselow, P. Kaufmann, I. Zorin, B. Heise, H. M. Chrzanowski, and S. Ramelow, "Frequency-domain optical coherence tomography with undetected mid-infrared photons," Optica **7**, 1729–1736 (2020).
18. C. Couteau, S. Barz, T. Durt, T. Gerrits, J. Huwer, R. Prevedel, J. Rarity, A. Shields, and G. Weihs, "Applications of single photons in quantum metrology, biology and the foundations of quantum physics," Nat. Rev. Phys. **5**, 354–363 (2023).
19. J. Fuenzalida, M. G. Basset, S. Töpfer, J. P. Torres, and M. Gräfe, "Experimental quantum imaging distillation with undetected light," Sci. Adv. **9**, eadg9573 (2023).
20. T. J. Herzog, J. G. Rarity, H. Weinfurter, and A. Zeilinger, "Frustrated two-photon creation via interference," Phys. Rev. Lett. **72**, 629–632 (1994).
21. M. V. Chekhova and Z. Y. Ou, "Nonlinear interferometers in quantum optics," Adv. Opt. Photon. **8**, 104–155 (2016).
22. A. Vanselow, P. Kaufmann, H. M. Chrzanowski, and S. Ramelow, "Ultra-broadband SPDC for spectrally far separated photon pairs," Opt. Lett. **44**, 4638–4641 (2019).
23. M. Arahata, Y. Mukai, B. Cao, T. Tashima, R. Okamoto, and S. Takeuchi, "Wavelength variable generation and detection of photon pairs in visible and mid-infrared regions via spontaneous parametric downconversion," J. Opt. Soc. Am. B **38**, 1934–1941 (2021).
24. P. Kaufmann, H. M. Chrzanowski, A. Vanselow, and S. Ramelow, "Mid-IR spectroscopy with NIR grating spectrometers," Opt. Express **30**, 5926–5936 (2022).
25. S. E. Harris, "Chirp and compress: toward single-cycle biphotons," Phys. Rev. Lett. **98**, 063602 (2007).
26. S. Sensarn, G. Y. Yin, and S. E. Harris, "Generation and compression of chirped biphotons," Phys. Rev. Lett. **104**, 253602 (2010).
27. A. Bruner, D. Eger, M. B. Oron, P. Blau, M. Katz, and S. Ruschin, "Temperature-dependent sellmeier equation for the refractive index of stoichiometric lithium tantalate," Opt. Lett. **28**, 194–196 (2003).
28. M. Levenius, V. Pasiskevicius, F. Laurell, and K. Gallo, "Ultra-broadband optical parametric generation in periodically poled stoichiometric $LiTaO_3$," Opt. Express **19**, 4121–4128 (2011).
29. A. Tanaka, R. Okamoto, H. H. Lim, S. Subashchandran, M. Okano, L. Zhang, L. Kang, J. Chen, P. Wu, T. Hirohata, S. Kurimura, and S. Takeuchi, "Noncollinear parametric fluorescence by chirped quasi-phase matching for monocycle temporal entanglement," Opt. Express **20**, 25228–25238 (2012).
30. D. B. Horoshko and M. I. Kolobov, "Towards single-cycle squeezing in chirped quasi-phase-matched optical parametric down-conversion," Phys. Rev. A **88**, 033806 (2013).
31. H. H. Lim, S. Kurimura, T. Katagai, and I. Shoji, "Temperature-dependent Sellmeier equation for refractive index of 1.0 mol% Mg-doped stoichiometric lithium tantalate," Japanese Journal of Applied Physics **52**, 032601 (2013).
32. M. Okano, H. H. Lim, R. Okamoto, N. Nishizawa, S. Kurimura, and S. Takeuchi, "0.54 μm resolution two-photon interference with dispersion cancellation for quantum optical coherence tomography," Sci. Rep. **5**, 18042 (2015).
33. B. Cao, M. Hisamitsu, K. Tokuda, S. Kurimura, R. Okamoto, and S. Takeuchi, "Efficient generation of ultra-broadband parametric fluorescence using chirped quasi-phase-matched waveguide devices," Opt. Express **29**, 21615–21628 (2021).
34. M. Hojo and K. Tanaka, "Broadband infrared light source by simultaneous parametric down-conversion," Sci. Rep. **11**, 17986 (2021).
35. J. Hirohashi, T. Tago, O. Nakamura, A. Miyamoto, and Y. Furukawa, "Characterization of GRIIRA properties in $LiNbO_3$ and $LiTaO_3$ with different compositions and doping," Proc. SPIE **6875**, 687516 (2008).
36. S. V. Tovstonog, S. Kurimura, T. Okubo, R. Kou, H. Nakajima, M. Motoya, and J. Ichikawa, "Violet light generation in quasi-phase-matched adhered ridge waveguide," Jpn. J. Appl. Phys. **47**, 4586–4588 (2008).
37. M. Charbonneau-Lefort, B. Afeyan, and M. M. Fejer, "Optical parametric amplifiers using chirped quasi-phase-matching gratings I: practical design formulas," J. Opt. Soc. Am. B **25**, 463–480 (2008).
38. G. E. Walrafen and S. R. Samanta, "Infrared absorbance spectra and interactions involving oh groups in fused silica," J. Chem. Phys. **69**, 493–495 (1978).